Plasma Sci. Technol. **25** (2023) 065501 (11pp) https://doi.org/10.1088/2058-6272/acafc1

Study of the 6.*x* nm short wavelength radiation spectra of laser-produced erbium plasmas for BEUV lithography

Tao WU (吴涛)[1,*], **Qian WANG** (王倩)[1], **Liuan CHEN** (陈柳安)[1] and **Peixiang LU** (陆培祥)[2]

[1] Hubei Key Laboratory of Optical Information and Pattern Recognition, School of Optical Information and Energy Engineering, Wuhan Institute of Technology, Wuhan 430205, People's Republic of China
[2] Guangdong Intelligent Robotics Institute, Dongguan 523808, People's Republic of China

E-mail: wutao@wit.edu.cn

Received 26 August 2022, revised 28 December 2022
Accepted for publication 3 January 2023
Published 28 February 2023

Abstract

Beyond extreme ultraviolet (BEUV) radiation with a wavelength of 6.*x* nm for lithography is responsible for reducing the source wavelength to enable continued miniaturization of semiconductor devices. In this work, the Required BEUV light at 6.*x* nm wavelength was generated in dense and hot Nd:YAG laser-produced Er plasmas. The spectral contributions from the 4p–4d and 4d–4f transitions of singly, doubly and triply excited states of Er XXIV–Er XXXII in the BEUV band were calculated using Cowan and the Flexible Atomic Code. It was also found that the radiative transitions between multiply excited states dominate the narrow wavelength window around 6.*x* nm. Under the assumption of collisional radiative equilibrium of the laser-produced Er plasmas, the relative ion abundance in the experiment was inferred. Using the Boltzmann quantum state energy level distribution and Gram–Charlier fitting function of unresolved transition arrays (UTAs), the synthetic spectrum around 6.*x* nm was finally obtained and compared with the experimental spectrum. The spatio-temporal distributions of electron density and electron temperature were calculated based on radiation hydrodynamic simulation in order to identify the contributions of various ionic states to the UTAs arising from the Er plasmas near 6.*x* nm.

Keywords: laser-produced plasmas, unresolved transition array, collisional radiative equilibrium

(Some figures may appear in colour only in the online journal)

1. Introduction

Extreme ultraviolet (EUV) sources have many important applications in various fields [1], especially in the semiconductor industry for high-volume manufacturing lithography and metrology tools [2–4]. Previously, researchers have been working on the 13.5 nm wavelength for more than a decade, and found that the output wavelength of the Sn target laser-produced plasma (LPP) source is around 13.5 nm, which is near the peak reflectivity of the Mo/Si multilayer mirrors [5–8]. The unresolved transition arrays (UTAs) of $4p^6 4d^n$–$4p^5 4d^{n+1}$ + $4d^{n-1}4f$ [9–12] from Sn VII–Sn XV are the dominant contributions to the 13.5 nm band. F Torretti *et al* [13] have studied the radiative contributions from multiply excited states of Sn plasma, and found that the contribution from singly excited states is small compared to multiply excited states. However, in order to advance the further development of next-generation nanolithography, researchers have started to investigate next-generation EUV sources with shorter output wavelengths better than 10 nm [14–16]. La/B_4C multilayer mirrors have been successfully prepared with a reflectivity of up to 58.6% in the vicinity of 6.7 nm [17], and their maximum theoretical reflectivity can exceed 70%. Therefore, researchers have become interested in LPP beyond-EUV (BEUV) sources and shifted the focus of their research to the 6.*x* nm band [18–21]. In the case of rare-

* Author to whom any correspondence should be addressed.

earth element targets, significant effort has been spent on developing a source for 6.*x* nm lithographic techniques to yield a smaller feature size [14, 22–25].

Recently, emission spectra based on Nd:YAG LPP in the 6.*x* nm band for lanthanide elements such as Tm [26] and Sm [27] have been investigated experimentally and theoretically. T Wu *et al* [28–32] have studied the BEUV radiation characteristics of Ho, Pb, Mo, Bi, and Yb LPPs in the range of 1–8 nm. A V Wezyk *et al* [33] have studied the EUV emission spectra of laser-generated plasma of Gd and Tb targets at wavelength of 6.*x* nm. The laser-assisted discharge plasma method has also been applied to generate strong radiation at the wavelength of 6.7 nm [34, 35]. Z Xie *et al* [36] have studied the EUV radiation spectra of dual-pulse laser-produced Gd plasma, and found that 4p–4d and 4d–4f resonance transitions from Gd XIX–Gd XXVII are the main contributions to the strong BEUV emission at 6.*x* nm. However, most researchers have tended to focus on the contributions of resonance transitions of 4p–4d and 4d–4f ($n = 4$)–($n = 4$), $\Delta n = 0$), and less in-depth studies of the open-4d shell transitions between multiply excited states such as doubly and triply excited states based on the configuration interaction (CI) have been reported.

In this study, plasmas were generated using a 1.064 μm Nd:YAG laser incident on an Er target in the experiment, and the time-integrated spectra of Er plasma in the 1.0–8.0 nm band were measured at different laser pulse energies and viewing angles. Theoretical transition spectra at the wavelength of 5.0–8.0 nm from Er XXIV–Er XXXII were obtained using Cowan [37] and the Flexible Atomic Code (FAC) [38]. The 4p–4d and 4d–4f transition spectra of singly excited state—ground state, doubly excited state—singly excited state, and triply excited state—doubly excited state based on the statistical theory of UTAs were analyzed. The structure of this paper is as follows. The experiment and collisional radiative equilibrium (CRE) model calculation are given in section 2. The energy level distributions for Er XXIV–Er XXXII, statistical analysis of ($n = 4$)–($n = 4$) spectral lines of unresolved transition arrays, and comparison of synthetic and experimental spectra are given in section 3. In section 4, a one-dimensional numerical simulation of Er laser plasma is presented. Finally, the conclusion of this paper is given in section 5.

2. Experiment and CRE model calculation

The experimental setup for laser plasma spectroscopy measurement of lanthanide element Er is shown in figure 1. A Q-switched backward-stimulated Brillouin scattering (SBS)-compressed Nd:YAG laser (EKSPLA SL312P) was used to generate maximum single pulse energy of 220 mJ, 150 ps full width at half maximum (FWHM) pulses at a wavelength of 1.064 μm. The laser pulses vertically illuminated the Er planar target in a vacuum chamber using a 10 cm focal length lens, and the focal spot radius was about 30 μm. The laser power density was varied from 5.2×10^{13} to 2.4×10^{13} W cm^{-2} by adjusting the magnitude of laser pulse energy. A flat-field grazing incidence spectrometer with 2400 lines mm^{-1} in combination with a back-illuminated sensitive x-ray charge-coupled device (CCD) camera that was placed directly behind this spectrometer was used to record the spectra from the plasma. The spectrometer for measuring EUV radiation pulses was placed at an angle of 60° or 30° with respect to the incident laser axis. Then the data were fed into the computer for real-time processing, and the resulting time-integrated recorded emission spectra of Er plasma in the wavelength band 1.0–8.0 nm are shown in figure 2. The measured radiation wavelength was calibrated using the known emission lines from laser-generated reference targets of Cu, Al_2O_3 and reaction-bonded silicon nitride (RBSN) Si_3N_4 plasmas with an uncertainty of 0.004 nm (rms value). The details of the calibration process can be obtained in reference [39].

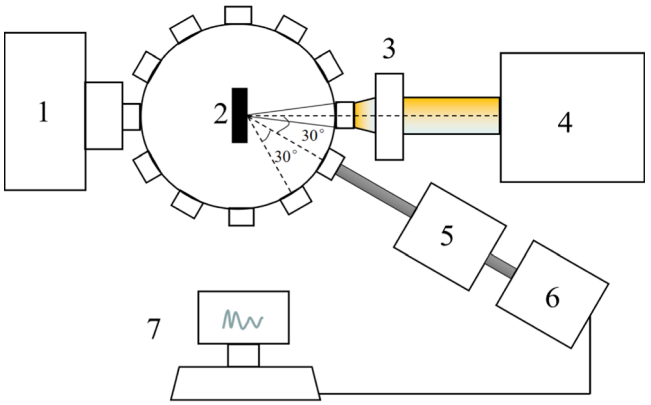

Figure 1. Experimental arrangement. 1: vacuum pump, 2: Er planar target, 3: focus lens, 4: 150 ps Nd:YAG laser, 5: x-ray spectrometer, 6: x-ray charge-coupled device (CCD), 7: computer.

The measured spectra for four incident laser pulse energies at two different viewing angles in the range of 1.0–8.0 nm are given in figure 2. There are continuous, superimposed UTA radiation and several strong discrete spectral lines shown in the spectra. With increasing laser power density, the spectra peak gradually increases, and the strong UTA peaks in the 2.0–5.0 nm region can be easily seen. As shown in figure 2, when the 150 ps laser Er plasma radiation is measured at the 60° angle, the BEUV radiation intensity is stronger compared to that at the 30° angle, which can be related to the radiation transport process of plasma. In the case of sub-nanosecond LPP, the plasma plume expansion velocity is higher along the target normal resulting in an ellipsoidal shape of the plasma plume [40]. The higher ionization stages responsible for the measured UTAs are generally generated at the hotter center of the plasma plume and the lower ion stages dominate close to the plume edge [41], which is also verified by our MED103 simulation in section 4. Because the plasma length is longer at the angle of 30°, the opacity effect by the low ion stage may considerably reduce the intensity, and the EUV radiation at the center of the plasma will be absorbed by the low-density plasma more than that at the angle of 60°. Moreover, these UTA peaks are subject to stronger self-absorption, and the jagged UTA radiation peaks are partially smoothed out.

In the experiment of the 1.064 μm laser-induced generation of EUV radiation from medium-Z to high-Z target plasmas, the electron temperature of the plasma is about 30–500 eV, and the electron density of plasma is of the order of the well-known critical electron density $n_{ec} = 10^{21}$ cm^{-3}

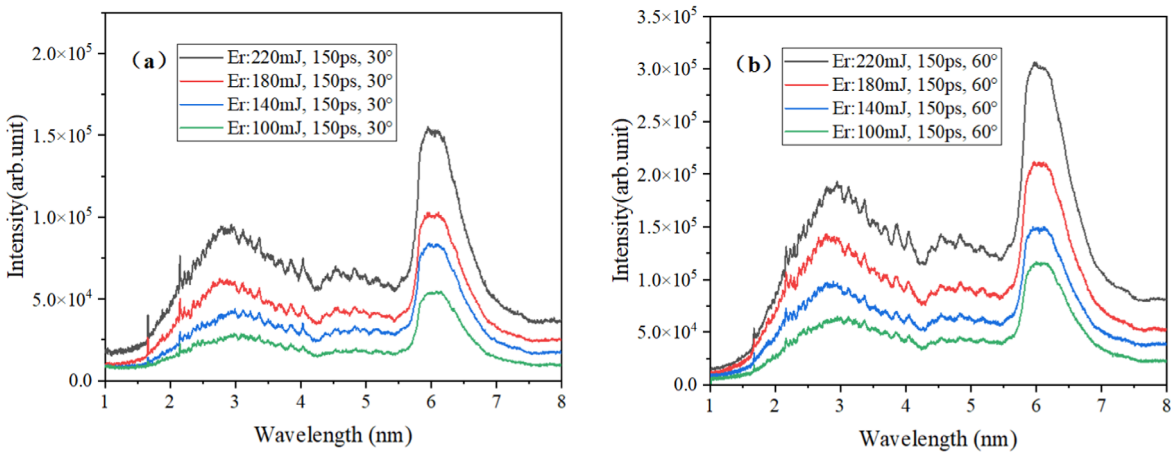

Figure 2. Experimental spectra from laser-produced Er plasma in the 1.0–8.0 nm wavelength band at different viewing angles of (a) 30°, (b) 60°.

($n_{ec} = 10^{21}/\lambda^2$ cm^{-3}, with λ in μm). Figure 3(a) shows the abundance of different multiply charged ions in the Er plasma versus electron temperature at the critical electron density of 10^{21} cm^{-3} using the CRE model, because the steady-state CRE model results can give a reasonable explanation for the ion abundance in the LPPs. It should be pointed out that the applicable conditions of the CRE model are as follows [42]. (i) The electron velocity distribution in the plasma is a Maxwell distribution. The electron density of laser plasma is very high, and the electron relaxation time is far less than other characteristic times, so it can be considered that the electron velocity satisfies the Maxwell distribution law. (ii) In the process of using the population density of ions of charge Z to estimate the population of ionization stage fractions in the quasi-steady state, the population density of ions of charge $(Z + 1)$ does not change greatly. As an approximation of the steady-state model used for the calculation, this condition is satisfied. (iii) The radiative opacity of the LPP is low. When the electron density is 10^{21} cm^{-3} and the electron temperature of the Er plasma is above 100 eV, this condition can be considered to be satisfied. According to the simulation results in section 4 of this paper, the plasma temperature greater than 100 eV is achieved at the peak of the laser pulse. As can be easily seen in figure 3, the most abundant ionic charge state will increase with increasing electron temperature in the range of 0–500 eV. Figure 3(b) shows the ionic populations at a specific electron temperature 197 eV and the critical electron density. As can be seen from figure 3, the open 4d subshell ions are evident in the range of electron temperature 100–400 eV, and there are only about five or six species of different multiply charged ions with obviously higher abundance in the Er LPPs at a specified plasma temperature.

3. Theoretical calculations and analysis

3.1. Energy level distributions of Er XXIV–Er XXXII

D Colombant *et al* [42] have given a local thermodynamic equilibrium (LTE) model, which is based on the energy conservation law, and the formula for estimating electron temperature of laser plasma is as follows:

$$T(\mathrm{eV}) \approx 5.2 \times 10^{-6} A^{1/5} [\lambda(\mu\mathrm{m})^2 \phi(\mathrm{W/cm^2})]^{3/5} \qquad (1)$$

where A is the atomic number, λ is the laser pulse wavelength, and ϕ is the laser flux. According to the LTE model, the calculation results show that the electron temperature and average ionization stage are around 2210 eV and 35 respectively for the 150 ps plasma at the maximum power density. It should be noted that this model is simple for the case of incompletely ionized targets and small radiation losses, in which only the ground state of each ion is taken into account. In reality, the electron temperature in the sub-nanosecond plasma is overestimated due to the neglection of the radiation losses, while the average ionization stage observed in the 150 ps LPP is always lower than that calculated as the time to reach the highest ion stage through successive ionization is too long for equilibrium to be established during the laser pulse lifetime. In order to develop the traditional model, a power balance model [43, 44] and a more detailed CR model [45] were proposed. According to the scaling relationships between the atomic number–electron temperature product dependence of the ionic charge states of the form $q = 0.64(AT_e)^{0.38}$ proposed in reference [43], we re-evaluate the electron temperature to be 182–400 eV by assuming the ionic charge state $q = 23$–31.

As shown in figure 3(a), with increasing electron temperature, the abundance of higher ionic stages and the average ionization degree increase in the Er plasmas. Some highly ionized Er ions in the plasmas may radiate x-rays with shorter wavelengths below 1.0 nm. The spectrometer used in the experiment measures the wavelength in the region of 1.0–8.0 nm, so the radiation of these highly ionized ions does not affect the measured results of the experimental spectra. As demonstrated in reference [13], the major contributions to the 13.5 nm band EUV light are from transitions between multi-excited states, and not from transitions between singly excited and ground states of Sn ions. It is estimated that these multiply excited states also dominate in the 6.x nm BEUV light due to the same strong $(n = 4)$–$(n = 4)$ transitions. Based on

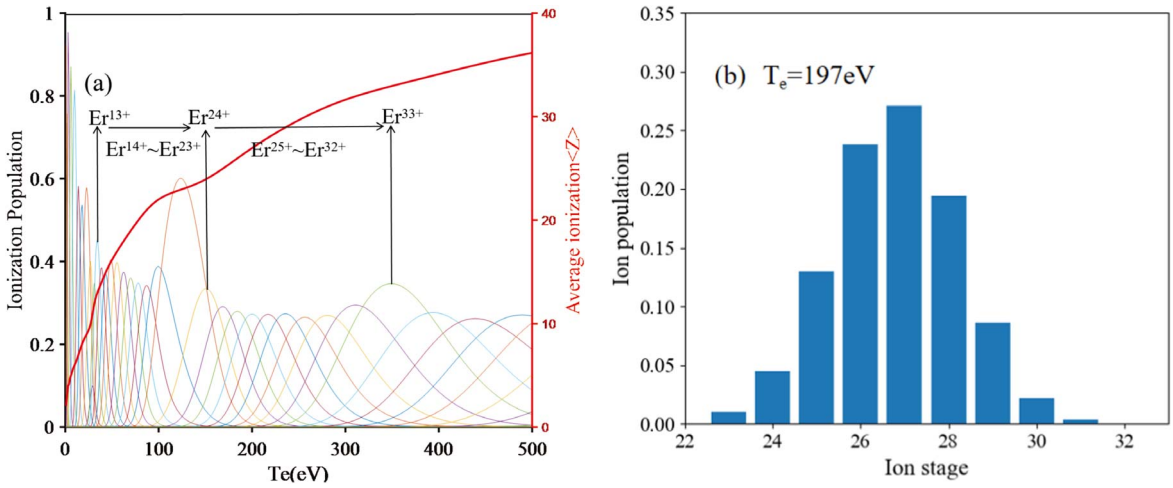

Figure 3. (a) Ionization stage populations and average ionization degree of Er plasma versus electron temperature calculated using the CRE model and (b) the ionic populations at a specified electron temperature $T_e = 197$ eV.

the theoretical atomic calculations, both the resonant 4p–4d and 4d–4f transition radiation and these transitions between doubly excited, triply excited and multiply excited states in Er XXIV–Er XXXII are studied in this section.

Figure 4 shows the energy level statistics of different electron configurations of Er XXVIII (left) and their number of energy levels (right). In the atomic structure calculations, it is not realistic to consider all electron configuration interactions of a specified ion. Therefore, only singly excited states, doubly excited states, and partial triply excited states with strong CI are taken into account in the calculations. As we continue to increase the number of higher excited configurations for CI, it is found that the calculation results are almost the same. The list of these configurations included in the calculations is presented in figure 4, and the lowest energy level of the ground state is taken as zero. Only the unclosed subshell electrons are described for the configurations in figure 4 without loss of generality. For example, the complete identification of electron configuration 4d5 should be $1s^2 2s^2 2p^6 3s^2 3p^6 4s^2 4p^6 4d^5$, and the electron configuration 4p5.4d6 should be $1s^2 2s^2 2p^6 3s^2 3p^6 4s^2 4p^5 4d^6$. The other electron configurations can be derived with the same rule, which is not presented here.

On the right panel of figure 4, type ① represents the resonance transition from singly excited state to ground state transitions, type ② represents excited transition from doubly excited state to singly excited state transitions, and type ③ represents excited transition from triply excited state to doubly excited state transitions. As shown in figure 4, the lowest number of energy levels for the ground configuration 4d5 is 37, while the number of energy levels of the multiply excited states is huge, and the maximum can be more than 10 000 energy levels. In addition to the stronger resonance transition, spontaneous radiative transitions will also occur between the quantum states of these highly excited states in the case of obeying the selection rule. Theoretical calculations show that for the open 4d shell of Er ions, the $(n = 4)$–$(n = 4)$ excited-excited transition arrays are also located in the 6.*x* nm wavelength region. For the radiative transitions of high-order moments such as electric quadrupole (E2) and magnetic dipole (M1), its radiative transition probability is several orders of magnitude lower than that of electric dipole (E1); hence, we do not discuss them in this work.

3.2. Analysis of (n = 4)–(n = 4) (Δn = 0) spectral lines of different transitions

Our calculation has shown that the 4p–4d and 4d–4f transitions of Er ions are responsible for the 6.*x* nm band. Therefore, without loss of generality, we take the most complicated Er XXVIII as an example for theoretical spectral analysis. Based on the energy level calculation of different electron configurations for Er XXVIII in section 3.1, the different transition spectra from 4p–4d+4d–4f of Er XXVIII are analyzed theoretically. Subsequently, the characteristics of the transitions are analyzed using the UTA statistical formula. The Cowan code solves the Schrödinger equation for a multi-electron atom in a multiconfiguration expansion approximation with relativistic corrections treated perturbatively. The FAC is based on the relativistic configuration interaction with independent particle basis wavefunctions. Since the FAC is an *ab initio* code without any empirical parameters, the simulated synthetic spectrum in section 3.3 is inferred from the FAC calculations and compared with the experimental spectrum in this paper. In order to identify the main ionization stages and features of radiative spectra in the range of 6.*x* nm band, the atomic radiation data using the FAC and Cowan codes are presented in tables 1 and 2. The ionization potentials calculated by FAC and Cowan are also compared in figure 5. As can be seen from the calculations, the differences calculated by FAC and Cowan are very small and the results of the two atomic structure calculations are basically consistent with each other.

In figure 6(a), the weighted radiative transition probability *gA* for each line emission of Er XXVIII is shown by red bars, and the spectrum convoluted with a Gaussian profile is shown by the solid blue line. The broadening factor is taken as the 0.01 nm to facilitate comparison with the instrumental

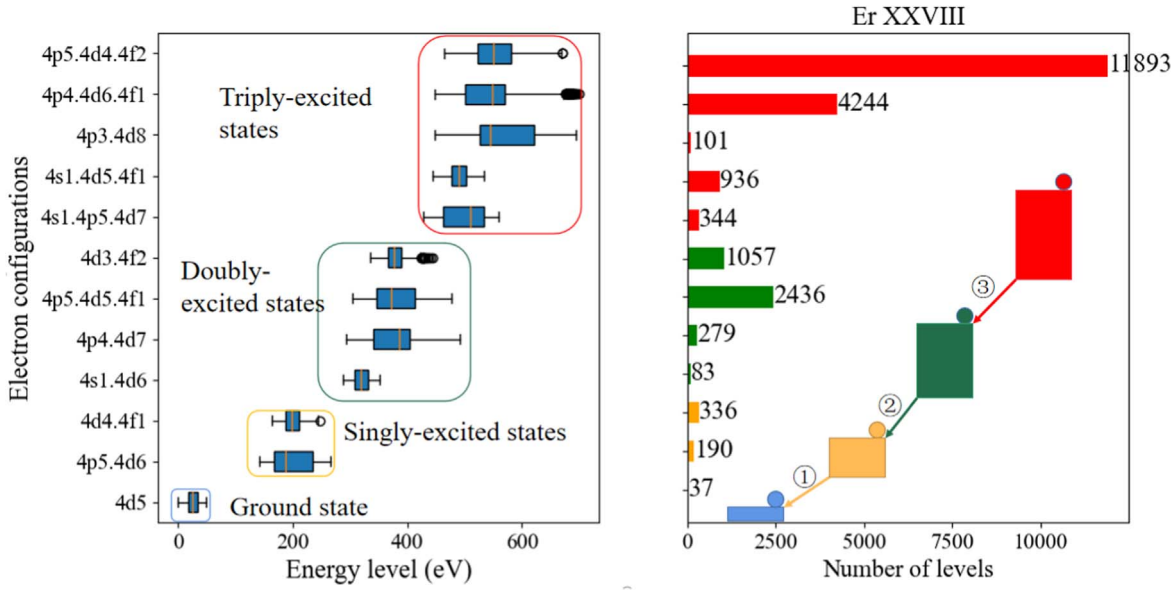

Figure 4. Energy level statistics of different electron configurations for Er XXVIII and the number of energy levels (blue is the ground state, orange is the singly excited state, green is the doubly excited state, and red is the triply excited state).

Table 1. UTA statistics of the 4p–4d and 4d–4f resonance transitions from Er XXIV–Er XXXII using FAC and Cowan.

				Mean λ (nm)				
Ion	Resonance transitions	Lines	$\sum gA$ (1/s)	FAC	Cowan	Std.	Skew	Kurt.
Er XXIV	4p6.4d9–4p5.4d10	4	9.57E+12	5.64	5.53	0.53	4.66	23.26
	4p6.4d9–4p6.4d8.4f1	78	1.12E+14	5.66	5.76	0.11	10.65	131.34
Er XXV	4p6.4d8–4p5.4d9	74	8.34E+13	5.72	5.59	0.51	4.72	24.65
	4p6.4d8–4p6.4d7.4f1	684	4.05E+14	5.78	5.83	0.14	8.07	80.81
Er XXVI	4p6.4d7–4p5.4d8	593	3.67E+14	5.79	5.66	0.44	4.97	29.30
	4p6.4d7–4p6.4d6.4f1	2536	8.10E+14	5.90	5.91	0.20	6.43	53.97
Er XXVII	4p6.4d6–4p5.4d7	1795	8.72E+14	5.75	5.73	0.41	4.84	31.33
	4p6.4d6–4p6.4d5.4f1	4960	1.49E+15	6.01	5.99	0.26	4.66	31.63
Er XXVIII	4p6.4d5–4p5.4d6	3104	1.08E+15	5.91	5.79	0.42	4.20	25.03
	4p6.4d5–4p6.4d4.4f1	4952	9.14E+14	6.15	6.11	0.35	3.40	16.84
Er XXIX	4p6.4d4–4p5.4d5	3168	1.06E+15	5.97	5.84	0.44	3.68	19.87
	4p6.4d4–4p6.4d3.4f1	2482	5.26E+14	6.32	6.24	0.41	2.12	8.00
Er XXX	4p6.4d3–4p5.4d4	1638	6.62E+14	6.02	5.90	0.46	3.26	16.01
	4p6.4d3–4p6.4d2.4f1	654	1.84E+14	6.56	6.38	0.48	1.14	3.46
Er XXXI	4p6.4d2–4p5.4d3	450	2.59E+14	6.06	5.96	0.50	2.85	11.88
	4p6.4d2–4p6.4d1.4f1	80	3.88E+13	6.92	6.79	0.48	0.17	2.00
Er XXXII	4p6.4d1–4p5.4d2	59	6.78E+13	6.09	6.03	0.58	2.25	7.16
	4p6.4d1–4p6.4f1	3	4.47E+12	7.23	7.12			

broadening in our experiment. Figure 6(b) shows the summed gA versus wavelength of the Er XXVIII 4p–4d and 4d–4f resonance transitions. Comparing with figure 6(b), it can be found that the Er XXVIII radiation spectra of resonance transition from 4p–4d and 4d–4f are mainly concentrated in the 6.x nm band.

Many references focus on the resonance transitions of $(n = 4)$–$(n = 4)$ $(\Delta n = 0)$ and less on the excited transitions between multiply excited states. In the LTE plasmas, the electronic energy level population of the ions can be considered to satisfy the Maxwell–Boltzmann distribution, and the highest probability of the electron configuration of the ions is at the ground state. However, in a high-temperature and high-density plasma, the excited-state energy level also has a certain population probability due to the presence of a large number of collisions. The multiply excited states should have a smaller population probability because of their higher energy level. However, due to the high statistical weights and a huge number of energy levels of these multiply excited states, which is several orders of magnitude larger than that of the singly excited state, it can be predicted that the number of spectral lines obeying the selection rule will increase sharply when the transition between multiply excited states occurs. Therefore, due to their large number of levels and high

Table 2. UTA statistics of the 4p–4d and 4d–4f transitions between excited states from Er XXV–Er XXXII using FAC and Cowan.

Ion	Excited transitions	Lines	$\sum gA$ (1/s)	Mean λ (nm)		Std.	Skew	Kurt.
				FAC	Cowan			
Er XXV	4p5.4d9–4p4.4d10	32	4.11E+13	5.61	5.56	0.61	3.83	28.60
	4p5.4d9–4p5.4d8.4f1	2253	7.67E+14	5.83	5.81	0.24	5.11	75.49
Er XXVI	4p5.4d8–4p4.4d9	690	2.27E+14	5.70	5.69	0.66	3.86	24.76
	4p5.4d8–4p5.4d7.4f1	19319	3.05E+15	5.89	5.86	0.31	3.43	40.10
Er XXVII	4p5.4d7–4p4.4d8	4760	7.96E+14	5.79	5.80	0.60	3.94	27.20
	4p5.4d7–4p5.4d6.4f1	71675	7.05E+15	5.96	5.97	0.37	2.73	34.38
Er XXVIII	4p5.4d6–4p4.4d7	15437	2.09E+15	5.89	5.92	0.53	3.50	26.60
	4p5.4d6–4p5.4d5.4f1	132129	1.03E+16	6.03	6.05	0.43	2.28	24.43
Er XXIX	4p5.4d5–4p4.4d6	28093	3.44E+15	5.96	5.98	0.51	3.26	23.64
	4p5.4d5–4p5.4d4.4f1	130459	9.93E+15	6.11	6.13	0.48	1.76	16.59
Er XXX	4p5.4d4–4p4.4d5	26653	3.69E+15	6.02	6.00	0.51	2.96	19.80
	4p5.4d4–4p5.4d3.4f1	70394	6.38E+15	6.20	6.23	0.54	1.35	11.07
Er XXXI	4p5.4d3–4p4.4d4	15269	2.69E+15	6.07	6.04	0.54	2.71	16.00
	4p5.4d3–4p5.4d2.4f1	18792	2.52E+15	6.32	6.36	0.60	0.89	6.88
Er XXXII	4p5.4d2–4p4.4d3	4529	1.21E+15	6.10	6.10	0.57	2.61	12.80
	4p5.4d2–4p5.4d1.4f1	2110	5.72E+14	6.54	6.57	0.64	0.10	4.20

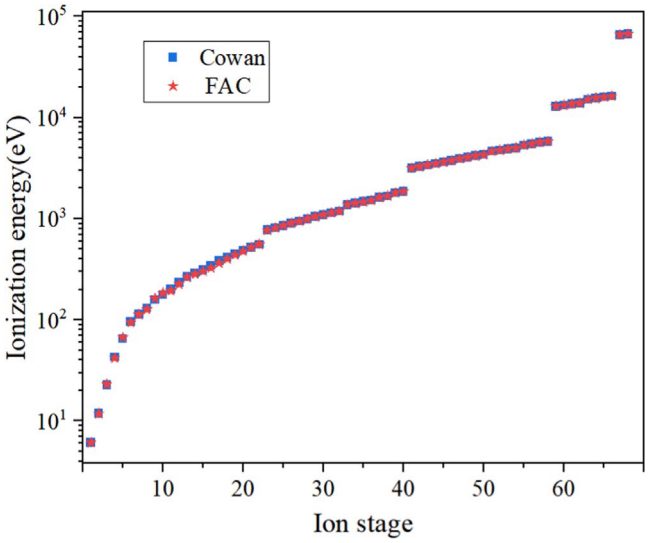

Figure 5. Comparison of ionization potentials of each Er ion using the FAC and Cowan codes.

statistical weights, the multiply excited configurations also have large populations despite the lower excitation probabilities. Little data for such excited to excited transitions are available for Er XXIV–Er XXXII. It is of great significance to study the radiative transitions between multiply excited states responsible for the 6.*x* nm band in the plasma.

Figure 7 shows the weighted radiative transition probability *gA*, the spectrum convoluted with a Gaussian profile, the *gA* versus wavelength of the excited–excited transitions between doubly and singly excited states from Er XXVIII 4p–4d and 4d–4f. The *gA* versus wavelength of the excited–excited transitions between triply and doubly excited states from Er XXVIII 4p–4d and 4d–4f is illustrated in figure 8. By comparison with figure 6, it can be easily seen that the number and summed intensity of emission lines between excited states are much larger, at several orders of magnitude larger compared to that of the resonance transitions. Therefore, it can be concluded that the transitions between multiply excited states are the dominant BEUV emission contributions to the relevant wavelength range in the laser-produced Er plasma.

Table 1 shows the UTA statistics of the 4p–4d and 4d–4f resonance transitions from Er XXIV–Er XXXII calculated by FAC and Cowan considering the strong CI. As can be seen from table 1, the *gA*-weighted average wavelength from 4p–4d and 4d–4f resonance transitions of Er XXIV–Er XXXII increases with increasing ionization stage. The skewness of the UTA statistics is all positive, indicating that the radiation spectra are biased toward the long-wavelength direction. The kurtosis values are generally much larger than 3, indicating that the peak type is much different from the Gaussian profile type. The spectral widths are mainly below 0.6 nm, indicating that the UTA spectral lines are highly concentrated.

The UTA statistics of 4p–4d and 4d–4f transitions between excited states from Er XXV–Er XXXII are given in table 2 using FAC and Cowan. By comparing tables 1 and 2, it is found that the number of spectral lines between the multiply excited states in the same ion is much larger, generally one order of magnitude larger compared to that of the resonance transition. It means that the radiative transitions contribution from multiply excited states to the 6.*x* nm cannot be neglected, which can far exceed the contributions from the resonance transition. As the number of open-4d-subshell electrons in the ground state is half a full shell, the number of spectral lines is highest. This phenomenon results from a sharp increase in the number of energy levels caused by the complex coupling between these electrons. The summed *gA* values can roughly reflect the intensity of the UTA contributing to the emission of relevant wavelength range. Hence, in general, these configurations corresponding to a half-filled 4d subshell at the ground state of $4d^5$ play a major role in the contribution to the 6.*x* nm band due to their large number of radiative spectral lines and high summed *gA* values.

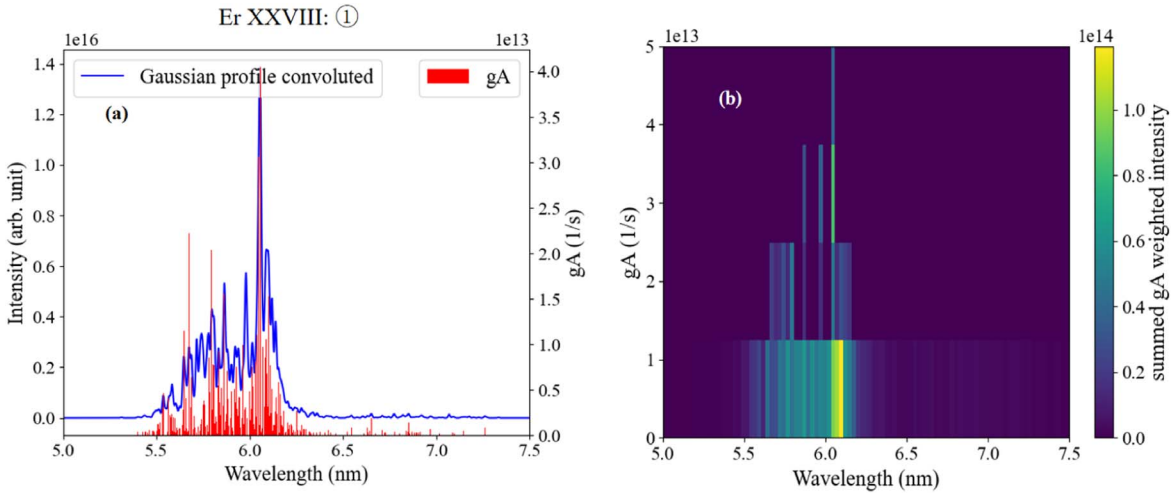

Figure 6. (a) Er XXVIII 4p–4d and 4d–4f resonance transitions and their spectra convoluted with a Gaussian profile, (b) line emission intensity distribution of the Er XXVIII 4p–4d and 4d–4f resonance transitions.

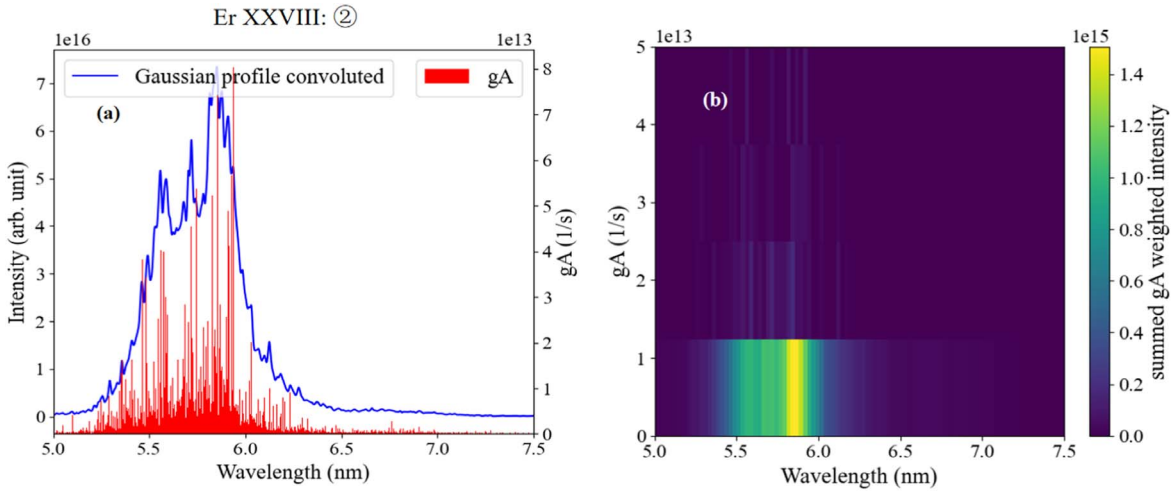

Figure 7. (a) Er XXVIII 4p–4d and 4d–4f radiative transitions from doubly to singly excited states and their spectra convoluted with a Gaussian profile, (b) line emission intensity distribution of Er XXVIII 4p–4d and 4d–4f excited transitions between doubly and singly excited states.

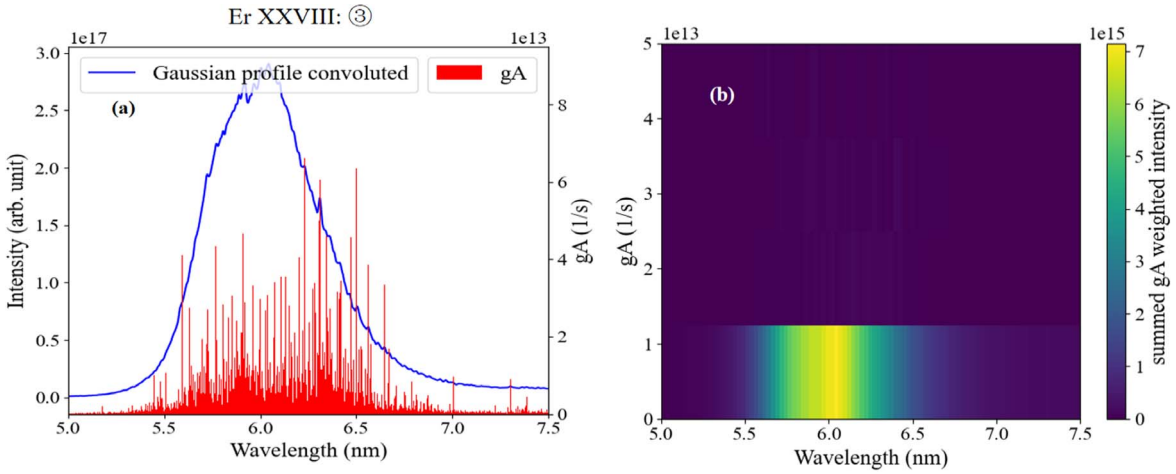

Figure 8. (a) Er XXVIII 4p–4d and 4d–4f radiative transitions from triply to doubly excited states and their spectra convoluted with a Gaussian profile, (b) line emission intensity distribution of Er XXVIII 4p–4d and 4d–4f excited transitions between triply and doubly excited states.

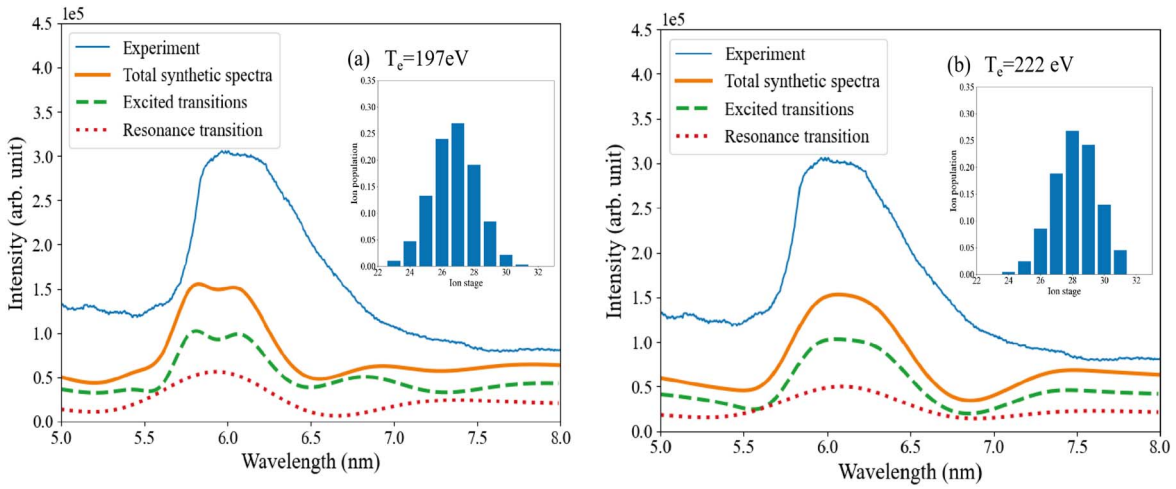

Figure 9. Comparison between the theoretical synthetic spectra and the experimental spectra in the 5.0–8.0 nm range at two electron temperatures (solid blue line is the experimental spectra, solid orange line is the total synthetic spectra, dashed green line is the synthetic spectra of excited to excited transitions, dotted red line is the synthetic spectra of resonance transition). (a) $T_e = 197$ eV, (b) $T_e = 222$ eV.

3.3. Comparison of synthetic and experimental spectra in the 6.x nm band

According to the results of the above theoretical calculation and analysis, it can be concluded that the dominant contribution to the 6.*x* nm band comes from the 4p–4d and 4d–4f transitions of different Er ions. The number of these spectral lines is extremely high, and the spectral lines are broadened by many effects: the instrumental width, the Doppler effect, collision broadening and so on. These numerous lines merge to form the UTAs, and then the spectral lines display quasi-continuous spectra which are recorded by the spectrometer. Line-by-line convolution calculation is not necessary, because it would occupy a lot of computer resources if all the spectral lines were taken into account. In order to analyze the statistical properties of the UTAs, the Gram–Charlier fitting function [46] can be used to holistically characterize this enormous number of spectral lines. The function reads:

$$f(\lambda) = \frac{\Omega}{\sigma\sqrt{2\pi}} \mathrm{e}^{-\frac{1}{2}u^2}\left[1 - \frac{\alpha_3}{2}\left(u - \frac{u^3}{3}\right) + \frac{\alpha_4 - 3}{24}(3 - 6u^2 + u^4)\right] \quad (2)$$

In equation (2), $u = (\lambda - \mu_1)/\sigma$, where μ_1 is the *gA*-weighted mean wavelength, σ is the standard deviation of wavelength, α_3, is skewness, α_4 is kurtosis, and Ω reflects the UTA subgroup intensity. The parameters of the UTA transition of various Er ions can be queried in tables 1 and 2. Based on the statistical parameters of 4p–4d and 4d–4f UTAs from various Er ions, the total synthetic spectra can be obtained by summing the Gram–Charlier fitting function given by equation (2). Using the Gram–Charlier fitting function, the comparison between the theoretical synthetic spectra and the experimental spectra in the relevant 6.*x* nm band (5.0–8.0 nm range) is shown in figure 9.

Specifically, figures 9(a) and (b) illustrate the comparison between the theoretical synthetic spectra of the total, resonance transitions, excited to excited transitions and the experimental spectra at two electron temperatures, where the inset shows the relative ionic stage population of the plasma. Note that it is hard to adopt the convolution calculation for each class of transitions in each ion stage due to the huge number of lines. The Gram–Charlier fitting function is used to obtain the synthetic spectra by weighting the ion population and summed *gA* of different classes of transitions from ion species. The summed *gA* values are deduced from the atomic structure calculations discussed above, while the ion population presented in the inset of figure 9 is based on the CRE model. For the purposes of comparison of electron temperature on the fitting spectra, the synthetic spectra based on the same critical electron density but for two associated plasma temperatures are illustrated in figures 9(a) and (b). It is not possible to fit a meaning distribution to the picosecond spectra based on other ion population assumptions with different electron density because the ion population changes very slowly with the electron density in the model. As shown in figure 9, it is made apparent that without the contributions from the multiply excited states it is not possible to fully explain the experimental spectrum. By comparing figures 9(a) and (b), the emission moves slightly to longer wavelengths when the electron temperature increases. This can be explained by the fact that the most abundant ion stage increases with increasing electron temperature based on the CRE model, and the higher ionization stages can result in the emissions of longer mean wavelength of UTAs, which is consistent with our calculations and the calculations in reference [47]. The same result is achieved as discussed above that the contribution of excited–excited transitions from 4p–4d and 4d–4f can exceed that of the resonance transition in the 6.*x* nm band. Moreover, the theoretical calculated wavelength is slightly shorter than the observation of experimental wavelength. This may be related to the electron configurations involved in the calculations—theoretically, all possible configurations should be considered—but this would consume a lot of computing resources, so our theoretical calculations only consider some electron configurations with the

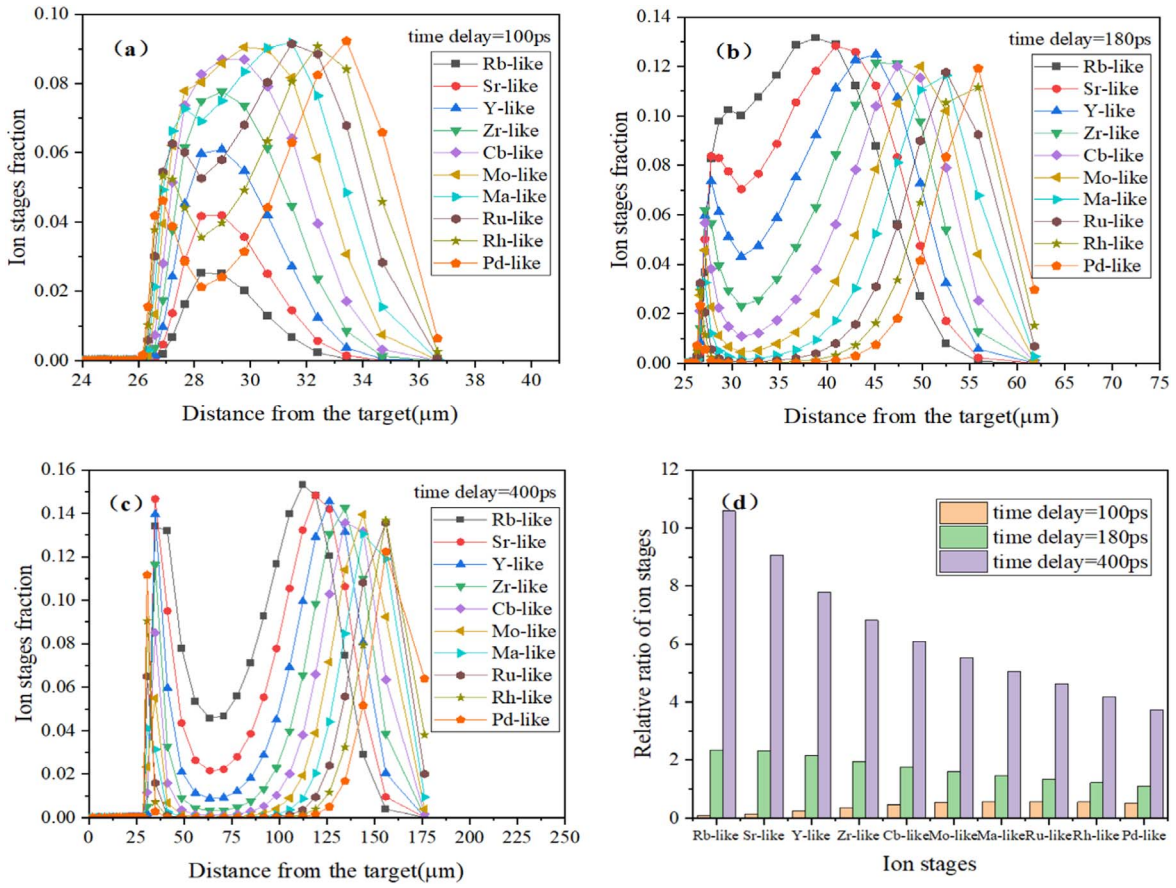

Figure 10. Variations of abundance for different ions at different delay times of (a) 100 ps, (b) 180 ps, (c) 400 ps, and (d) spatio-temporal integration of the relative abundance of different ions at different delay times.

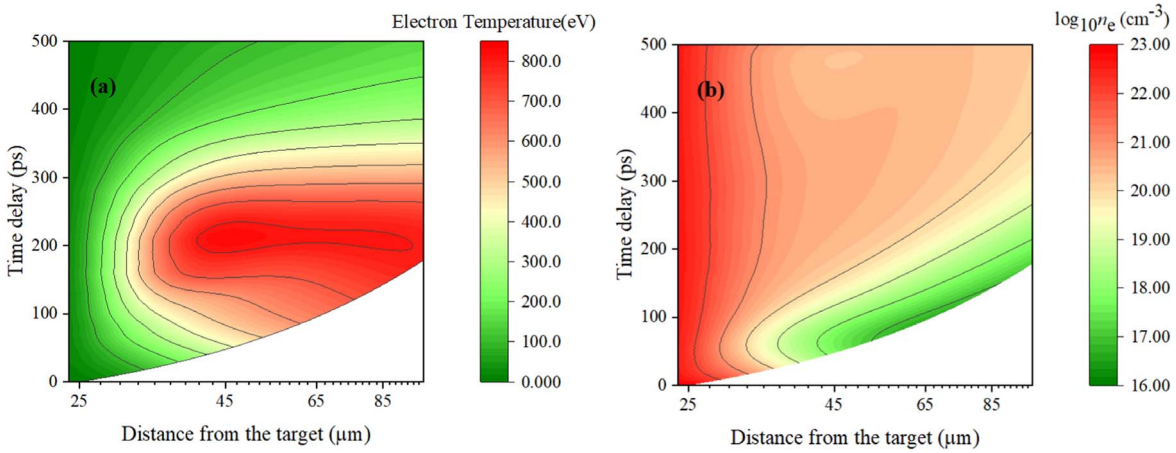

Figure 11. Numerical simulation results under our experimental conditions. (a) Electron temperature, (b) electron density.

strongest CI. Overall, the level of agreement with experimental observations is satisfactory.

4. Simulation

The experimental parameters were applied in the one-dimensional laser plasma simulation package MED103 [48] for the identification of the plasma properties. The basic parameters were set as follows: laser wavelength 1.064 μm, pulse FWHM 150 ps, peak power of the pulsed laser 5.2×10^{13} W cm^{-2}, and thickness of the planar Er target 25 μm. The numerical simulation results are shown in figures 10 and 11.

In figures 10(a)–(c), it can be seen that the traces of Er ions show a two-peak behavior at high laser intensity irradiation. The results show that the first peak becomes increasingly dominant and the second peak becomes more prominent with increasing time delay. The two-peak behavior can be caused by three possible mechanisms:

(i) recombination kinetics, (ii) lateral heat conduction, and (iii) ablation by x-ray radiation transport [49]. Energy transport simulations of Er plasma show that the results are consistent with those by a two-zone plasma model consisting of a high-temperature electron thermal transport region and a low-temperature high-density radiation transport region. There is a long high-temperature and flat ion density corona region when the pulse laser focuses on the target surface, and the plasma temperature is essentially spatially uniformly distributed in this region. The results enable the applicability of a single-density, single-temperature approach for the calculated charge state abundance. In figure 10(d), it can be seen that the open-4d-subshell ions of Er XXIV–Er XXXII that can generate the UTA transitions of 4p–4d+4d–4f are obtained. After comparison with tables 1 and 2, it can be found that the spectra of Er XXIV–Er XXXII provide the dominant contributions and corresponding transitions for the experimental spectrum in the 6.*x* nm band.

As shown in figure 11(a), when the laser beam is focused on the target surface it ionizes the atoms and produces an expanding outward plasma. The plasma temperature reaches a peak at about 200 ps in this situation, and then the plasma temperature gradually decreases. It can be found that soft x-ray radiation is mainly generated in the period from 100 to 300 ps. By comparison with figure 3, it is illustrated that the electron temperature along the direction perpendicular to the target surface can reach 800 eV, which fully satisfies the condition of generating highly charged Er ions for soft x-ray radiation. It is found that the high electron temperature region in figure 11(a) is associated with an electron density range from 10^{19} to 10^{21} cm^{-3} by comparison with figure 11(b), which is also the main region of laser energy absorption known as the corona. The simulation results show that plasma with obviously high abundance of highly charged Er ions can be generated at the peak of laser pulse intensity, which is located about 60 μm away from the target surface and plays a leading role in the contribution to the 6.*x* nm band.

5. Conclusions

Experimentally, a picosecond Nd:YAG pulsed laser was used to generate plasma on a high-purity planar Er target in a vacuum chamber, and Er plasma emission spectra from 1.0 to 8.0 nm were recorded by a soft x-ray spectrometer and CCD. Theoretically, the plasma transition spectra of singly, doubly, and triply excited states from Er XXIV–Er XXXII 4p–4d and 4d–4f were calculated using FAC and Cowan codes and analyzed using UTA statistical theory. Using the Gram–Charlier fitting function of UTAs, the theoretical synthetic spectrum around 6.*x* nm was given and compared with the experimental spectrum, with a fine agreement between them obtained. It was found that, contrary to the conclusions of the existing literature, these radiative transitions between multiply excited states are the dominant contribution to the 6.*x* nm band. Using the 1D Lagrangian hydrodynamic code MED103 package, the spatio-temporal distributions of electron temperature and electron density were obtained under the experimental parameter conditions. The simulation results enable the applicability of a single-density, single-temperature approach for the charge state abundance calculation and synthetic spectra simulation. It should be pointed out that based on the 1D simulation code MED103, the rough temporal-spatial resolved electron temperature, density and ion stages fraction can be obtained according to the experimental setup, which makes it possible to simulate the temporal-spatial resolved spectrum combined with the atomic spectral computation code. However, both the elaborate simulation results for the complex process of LPP and the not easily obtained temporal-spatial resolved soft x-ray spectra are the key to the problem. It is of great significance to compare the temporal-spatial resolved experimental spectra with the more complicated magnetohydrodynamic simulations in which plasma effects are involved. In this paper, since the soft x-ray spectra are time- and space-integrated and measured, we have presented a simple simulation of the spectrum in this earlier work using the single-electron density and single-electron temperature approach. This provides a theoretical and experimental basis for future research on 6.*x* nm LPP-BEUV lithography sources.

Acknowledgments

The authors acknowledge the support from Guangdong Major Project of Basic and Applied Basic Research (No. 2019B030302003).

ORCID iDs

Tao WU (吴涛) https://orcid.org/0000-0002-2279-680X

References

[1] Attwood D T 2000 *Soft X-rays and Extreme Ultraviolet Radiation: Principles and Applications* (Cambridge: Cambridge University Press)
[2] Basko M M 2016 *Phys. Plasmas* **23** 083114
[3] Su M G *et al* 2017 *Sci. Rep.* **7** 45212
[4] Torretti F *et al* 2018 *J. Phys. B: At. Mol. Opt. Phys.* **51** 045005
[5] Roy A *et al* 2014 *Appl. Phys. Lett.* **105** 074103
[6] Torretti F *et al* 2020 *J. Phys. D: Appl. Phys.* **53** 055204
[7] Versolato O O 2019 *Plasma Sources Sci. Technol.* **28** 083001
[8] Huang Q S *et al* 2017 *Appl. Phys. Rev.* **4** 011104
[9] Fomenkov I *et al* 2017 *Adv. Opt. Technol.* **6** 173
[10] Windberger A *et al* 2016 *Phys. Rev. A* **94** 012506
[11] Colgan J *et al* 2017 *High Energy Density Phys.* **23** 133
[12] Torretti F *et al* 2017 *Phys. Rev. A* **95** 042503
[13] Torretti F *et al* 2020 *Nat. Commun.* **11** 2334
[14] Sasaki A *et al* 2010 *Appl. Phys. Lett.* **97** 231501
[15] Churilov S S *et al* 2009 *Phys. Scr.* **80** 045303
[16] Amano R *et al* 2018 *Jpn. J. Appl. Phys.* **57** 070311
[17] Chkhalo N I *et al* 2013 *Appl. Phys. Lett.* **102** 011602
[18] Yin L *et al* 2016 *Phys. Rev. Appl.* **6** 034009
[19] Kilbane D and O'Sullivan G 2010 *J. Appl. Phys.* **108** 104905
[20] Cummins T *et al* 2012 *Appl. Phys. Lett.* **100** 061118
[21] Otsuka T *et al* 2010 *Appl. Phys. Lett.* **97** 111503

[22] Ohashi H *et al* 2014 *J. Appl. Phys.* **115** 033302
[23] Tian Y *et al* 2016 *AIP Adv.* **6** 035108
[24] Yoshida K *et al* 2015 *Appl. Phys. Lett.* **106** 121109
[25] Higashiguchi T *et al* 2013 *Opt. Express* **21** 31837
[26] Sheil J *et al* 2017 *J. Phys. B: At. Mol. Opt. Phys.* **50** 065006
[27] Lokasani R *et al* 2018 *J. Phys. B: At. Mol. Opt. Phys.* **51** 215001
[28] Wu T *et al* 2020 *J. Phys. B: At. Mol. Opt. Phys.* **53** 225701
[29] Wu T *et al* 2017 *Opt. Commun.* **385** 143
[30] Wu T *et al* 2018 *Spectrosc. Spectral Anal.* **38** 692 (in Chinese)
[31] Wu T *et al* 2020 *Plasma Sci. Technol.* **22** 105503
[32] Wu T *et al* 2016 *J. Phys. B: At. Mol. Opt. Phys.* **49** 035001
[33] von Wezyk A *et al* 2019 *J. Phys. D: Appl. Phys.* **52** 505202
[34] Xu Q *et al* 2019 *Symmetry* **11** 050658
[35] Wang J W *et al* 2021 *Opt. Laser Technol.* **138** 106904
[36] Xie Z *et al* 2022 *Acta Phys. Sin.* **71** 035202 (in Chinese)
[37] Cowan R D 1981 *The Theory of Atomic Structure and Spectra* (Berkeley: University of California Press)
[38] Gu M F 2008 *Can. J. Phys.* **86** 675
[39] Dinh T H *et al* 2016 *Rev. Sci. Instrum.* **87** 123106
[40] Filevich J *et al* 2003 *Phys. Rev. E* **67** 056409
[41] O'Gorman C *et al* 2012 *Appl. Phys. Lett.* **100** 141108
[42] Colombant D and Tonon G F 1973 *J. Appl. Phys.* **44** 3524
[43] Shimada Y *et al* 2019 *AIP Adv.* **9** 115315
[44] Kawasaki H *et al* 2020 *AIP Adv.* **10** 065306
[45] Sasaki A *et al* 2016 *AIP Adv.* **6** 105002
[46] Gilleron F *et al* 2008 *Phys. Rev. E* **77** 026708
[47] Kilbane D 2011 *J. Phys. B: At. Mol. Opt. Phys.* **44** 165006
[48] Djaoui A A user guide for the laser plasma simulation code: MED103[EB/OL]. 2020-01-06. http://inspirehep.net/files/ad38345b92c364544b8cb515390afede
[49] Tsui Y Y 1992 Hydrodynamics of UV laser-produced plasma *PhD Thesis* University of Alberta, Edmonton